New observations of the distribution, morphology, and dissolution dynamics of cryogenic gypsum in the Arctic Ocean

Jutta Erika Wollenburg[1*], Morten Iversen[1,2], Christian Katlein[1], Thomas Krumpen[1], Marcel Nicolaus[1], Giulia Castellani[1], Ilka Peeken[1], Hauke Flores[1]

[1]Alfred-Wegener-Institut Helmholtz-Zentrum für Polar- und Meeresforschung, D-27570, Bremerhaven, Germany

[2]MARUM and University of Bremen, D-27359, Bremen, Germany

[*]Corresponding author and requests for materials should be addressed to J.E.W. (email: Jutta.Wollenburg@awi.de)

12   **Abstract**

13   To date observations on a single location indicate that cryogenic gypsum ($Ca[SO_4]\cdot 2H_2O$) may

14   constitute an efficient but hitherto overlooked ballasting mineral enhancing the efficiency of

15   the biological carbon pump in the Arctic Ocean. In June-July 2017 we sampled cryogenic

16   gypsum under pack-ice in the Nansen Basin north of Svalbard using a plankton net mounted

17   on a Remotely Operated Vehicle (ROVnet). Cryogenic gypsum crystals were present at all

18   sampled stations, which suggested a persisting cryogenic gypsum release from melting sea ice

19   throughout the investigated area. This was supported by a sea-ice backtracking model

20   indicating that gypsum release was not related to a specific region of sea ice formation. The

21   observed cryogenic gypsum crystals exhibited a large variability in morphology and size, with

22   the largest crystals exceeding a length of 1 cm. Preservation, temperature and pressure

23   laboratory studies revealed that gypsum dissolution rates accelerated with increasing

24   temperature and pressure, ranging from 6% d^{-1} by mass in Polar Surface Water (-0.5 °C) to

25   81% d^{-1} by mass in Atlantic Water (2.5 °C at 65 bar). When testing the preservation of gypsum

26   in Formaldehyde-fixed samples we observed immediate dissolution. Dissolution at warmer

27   temperatures and through inappropriate preservation media may thus explain why cryogenic

28   gypsum was not observed in scientific samples previously. Direct measurements of gypsum

29   crystal sinking velocities ranged between 200 and 7000 m d^{-1}, suggesting that gypsum-loaded

30   marine aggregates could rapidly sink from the surface to abyssal depths, supporting the

31   hypothesised potential of gypsum as a ballasting mineral in the Arctic Ocean.

32

35

1 Introduction

37 Climate change in the Arctic Ocean has led to a drastic reduction of summer sea ice extent as
38 well as to a significant thinning of the sea ice (Kwok, 2018; Kwok and Rothrock, 2009). Sea
39 ice strength has reduced, and increased deformation and fractionation result in a progressively
40 increasing sea ice drift speed (Docquier et al., 2017) and sea-ice export. Over the past decades
41 the ice export via the Fram Strait alone has increased by 11% per decade during the
42 productive spring and summer period (Smedsrud et al., 2017). An increasing amount of sea
43 ice produced in the East Siberian and Laptev Sea melts over the adjacent continental slopes or
44 in the central Arctic Ocean (Krumpen et al., 2019). Overall, the Arctic Ocean sea ice cover
45 has shifted to a predominantly seasonal ice cover. However, although the majority of sea ice
46 diminishes during late summer, the amount of sea ice produced in autumn to winter
47 progressively increases (Kwok, 2018).

48 Large-scale transformations in the seasonal sea-ice cover impact the physical, chemical and
49 biological dynamics of the sea ice-ocean system. However, especially the interactions of
50 physical-chemical processes within the sea ice and pelagic to benthic biological processes
51 have only received little attention. Of particular importance are poorly soluble minerals
52 precipitated within the brine channels of sea ice which, once released, may ballast organic
53 material sinking to the sea-floor. The changing icescape with more leads and the thinner
54 Arctic sea ice allows increasing light penetration into the under-ice surface water (Katlein et
55 al., 2015; Nicolaus et al., 2013; Nicolaus et al., 2012), supporting fast-growing and often
56 massive under-ice phytoplankton blooms (Arrigo et al., 2012; Arrigo et al., 2014; Assmy et
57 al., 2017). A recent study reported on a sudden export event of an under-ice bloom of the
58 'unsinkable alga' *Phaeocystis,* caused by the ballasting effect of cryogenic gypsum released
59 from melting sea ice (Wollenburg et al., 2018a). This single event was the first and only
60 report of cryogenic gypsum release in the Arctic Ocean. Moreover, this sea ice precipitation
61 of cryogenic gypsum has never been recorded in Arctic sediments, sediment traps or other
62 field studies.

63 When sea ice forms, the concentrations of dissolved ions in brine increase, and depending on
64 the temperature of sea ice, a series of minerals (ikaite, mirabilite, hydrohalite, gypsum,
65 hydrohalite, sylvite, $MgCl_2$, Antarcticite) precipitate (Butler, 2016; Butler and Kennedy, 2015;
66 Geilfus et al., 2013; Golden et al., 1998; Wollenburg et al., 2018a). Once released into the
67 ocean, gypsum is considered to be the most stable of the cryogenic precipitates (Butler et al.,

68   2017; Strunz and Nickel, 2001). Sea ice-derived cryogenic gypsum was first described by

69   Geilfus et al. (2013), in a comprehensive work on the chemical, physical, and mineralogical

70   aspects of its precipitation in experimental and natural sea ice off Greenland. According to

71   FREZCHEM, a chemical–thermodynamic model that was developed to quantify aqueous

72   electrolyte properties at sub-zero temperatures, cryogenic gypsum can precipitate at

73   temperatures below −18 °C, and within a small temperature window between −6.5 and −8.5

74   °C (Geilfus et al., 2013; Marion et al., 2010; Wollenburg et al., 2018a). However,

75   measurements on the stoichiometric solubility products showed that gypsum dynamics in ice–

76   brine equilibrium systems strongly depend on the solubility and precipitation of hydrohalite

77   and mirabilite (Butler, 2016; Butler et al., 2017). So far gypsum precipitation in experimental

78   setups were only observed at temperatures between -7.1 and -8.2 °C, and not in the lower

79   temperature range (Butler, 2016; Butler et al., 2017). Moreover, as Arctic sea ice rarely

80   reaches temperatures lower than -18 °C, cryogenic gypsum is more likely precipitated within

81   the higher temperature window in the Arctic Ocean (Wollenburg et al., 2018a).

82   A model applied to understand the gypsum release event of 2015 showed that the ice floe was

83   too warm when it started to form and identified December to February as the most likely time

84   span for gypsum precipitation (Wollenburg et al., 2018a). Due to the absence of a downward

85   brine flux in this advanced phase of sea ice formation, gypsum crystals likely remain trapped

86   in the ice until spring. In the absence of sufficient field observations gypsum release from sea

87   ice is expected to peak at the beginning of the melting season, when sea ice warms to

88   temperatures above -5 °C. This temperature marks the transition in the fluid transport

89   capacities of sea ice allowing brine water and included crystals to be released into the water

90   column (Golden et al., 1998). However, in lack of any extensive, year-round field studies our

91   knowledge depends on models, kinetics and two single field observations (Geilfus et al.,

92   2013; Wollenburg et al., 2018a). There are no studies on sea ice-derived cryogenic gypsum

93   crystal morphologies and its stability in seawater. It is unclear whether gypsum just

94   precipitates during the assumed peak in December to February or whether it continues to

95   grow in remaining brines during sea ice drift.

96   In this study, we systematically investigated the occurrence of cryogenic gypsum release from

97   sea ice in spring 2017 with special emphasis on the morphological properties of the crystals.

98   Varieties of cryogenic gypsum crystal morphologies are described and illustrated. The

99   sampled gypsum crystals were further subjected to various laboratory experiments. Hereby,

100   we investigated the dissolution behaviour over typical depth- and temperature ranges of the

101   Arctic water column and in Formaldehyde solution typically used for biological sampling

102   preservation. We also made direct measurements of the size-specific sinking speed of

103   individual gypsum crystals. These experiments were conducted to answer the question, why

104   cryogenic gypsum has not previously been observed in field studies and if it qualifies as

105   ballast mineral.

106

107

108   **2   Material and Methods**

109   **2.1   Gypsum sampling with the ROVnet and on-board treatment**

110   RV *Polarstern* expedition PS 106 (June-July 2017) in the early melting season gave the

111   opportunity to systematically study the occurrence of cryogenic gypsum release and the

112   morphological properties of gypsum crystals in the area north of Svalbard and on the Barents

113   Sea shelf (Fig. 1A; Table 1).

114   Cryogenic gypsum was sampled from the upper 10 m of the under-ice water at four stations

115   distributed throughout the expedition area (Fig. 1A; Table 1). The first part of the expedition

116   (PS106/1) consisted of a drift study to the north of Svalbard, during which the vessel was

117   anchored to an ice floe (station 32). This ice floe was revisited 6 weeks later at the end of the

118   expedition (PS106/2) (station 80). During the second part of the expedition (PS106/2),

119   cryogenic gypsum was collected over the western Barents Sea (station 45) and in the Nansen

120   Basin to the north-east of Svalbard (station 66).

121   Gypsum crystals were sampled with a plankton net mounted on a remotely operated vehicle

122   (ROVnet, Fig. S1). The ROVnet consists of a Polycarbonate frame with an opening of 40 cm

123   by 60 cm, to which a zooplankton net with a mesh size of 500 μm was attached (Flores,

124   2018). For gypsum sampling, a handmade nylon net with an opening of 10 cm by 15 cm and a

125   mesh size of 30 μm was mounted in the zooplankton net opening. The concentrated

126   particulate material of the small nylon net was collected in a 2 L polyethylene bottle attached

127   to the cod end of the net. A gauze-covered window in the cod-end bottle allowed seawater to

128   drain off. Both nets were mounted on the aft end of a M500 (Ocean Modules, Sweden)

129   observation class ROV carrying an extensive sensor suite described in Katlein et al. (2017).

130   After each ROVnet deployment, the nets were rinsed with ambient sea-water to concentrate

131   the sample in the cod end of the net. The ROVnet sampled horizontal profiles in the water

132   directly below the sea ice. Standard ROVnet profiles were conducted at the ice-water

133   interface, at 5 m and at 10 m depth. The distance covered by each profile ranged between 300

134   and 600 m. At station 32, the 10 m profile was aborted due to technical failure, and at station

135   80 no 5 m profile was sampled due to time constraints, and the subsurface sample was

136   discarded due to handling failure (Table 1).

137   The concentrated particulate material collected in the cod-end bottle of the gypsum sampling

138   net was mixed with a sample equivalent volume of 98% ethanol, and stored at 4 °C until

139   further analyses (Wollenburg et al., 2018a).

140   At ROVnet sampling stations, ice thickness was estimated through thickness drill holes with a

141   tape measure. To characterize the properties of the ice floes sampled on the floe-wide scale,

142   ice thickness surveys were conducted at each sampling station with a GEM2 (Geophex)

143   electromagnetic induction ice-thickness sensor (Katlein et al., 2018).

144   **2.2   Initial analyses of ROVnet samples**

145   In the home laboratory the samples were rinsed onto a 32 μm mesh using fresh water. The

146   samples were then oven-dried at 50°C for 20 hours. The remaining crystals were transferred

147   into pre-weighed micropaleontological slides, and their weight was determined with a high-

148   precision Sartorius SE2 ultra-microbalance. Under a Zeiss Axio Zoom V16 microscope,

149   pictures were taken with an Axiocam 506 colour camera. We made both overview images of

150   the whole sample and detailed images of individual crystals. From all samples and crystal

151   morphologies, individual crystals were analysed using Raman microscopy, which confirmed

152   that the crystals were gypsum (Wollenburg et al., 2018a). As in some samples both, very large

153   and very small crystals (Figs. S3-S4) were observed, the >32 μm samples were dry-sieved

154   over a 63 μm analysis sieve. The length and width of the cryogenic gypsum crystals in the

155   size fractions >32<63 μm and >63 μm was determined with the software application ImageJ

156   on 50 crystals in each sample and size fraction (Schneider et al., 2012) (Tab. 2).

157   **2.3   Initial analyses of ice cores**

158   At all ice stations, sea ice cores for archive purposes and for further measurement of bottom

159   communities were drilled with a 9 cm diameter ice corer (Kovacs Enterprise) and stored at -

160   20°C (Peeken, 2018). One ice-core from station 80 and four bottom slices (10 cm) of ice-

161   cores from station 45 were studied to investigate the gypsum crystal morphologies within sea

162   ice. Each section was transferred into a measuring jug with lukewarm tap water for approx.

163   two seconds, and then the jug was emptied over a 32 μm analysis sieve, and repeatedly

164   refilled. This process was continued until all ice was melted. With the aid of a hand shower

165   and a wash bottle the residue on the sieve was rinsed and transferred into a 30 μm mesh-

166   covered funnel, dried and transferred into a micropaleontological picking tray for inspection

167   and documentation. For storage, the residue was transferred into pre-weighed labelled

168   micropaleontological slides.

169   **2.4   Dissolution experiments**

170   The aim of our dissolution experiments was to investigate the persistence of gypsum crystals

171   against dissolution in the Arctic water column (water mass trials) and under common

172   biological sample treatment (Formaldehyde trial).

173   Dissolution experiments were carried out on individual gypsum crystals collected from

174   ROVnet samples. Hereby, 5 cryogenic gypsum crystals with different crystal morphologies,

175   and from both size fractions were used in each reaction chamber. Before the start and after the

176   termination of each experiment, pictures of the cryogenic gypsum crystals used were taken

177   with an Axiocam 506 colour camera under a Zeiss Axio Zoom V16 microscope. The weight

178   of the crystals before and after each treatment was determined with a high-precision Sartorius

179   SE2 ultra-microbalance after they had been transferred into a pre-weighted silver boat. The

180   experimental running time of each experiment was 24 hours.

181   **2.4.1   Water mass trials**

182   The experiments to simulate dissolution within the different water masses and hydrostatic

183   pressure regimes of the Arctic Ocean were carried out with high-pressure chambers installed

184   in a cooling table (Wollenburg et al., 2018b). With a high-pressure pump (ProStar218 Agilent

185   Technologies), peak tubing, and multiple titanium valves a continuous isobaric and isocratic

186   one-way seawater flow of 0.3 ml/min was directed through a set of four serially arranged

187   high-pressure chambers each with an internal volume of 0.258 ml (Wollenburg et al., 2018b).

188   This setup allowed for dissolution experiments at defined pressures and temperatures

189   (Wollenburg et al., 2018b). For the experiments, we used sterile-filtered (0.2 μm mesh) North

190   Sea water that was adjusted to a salinity of 34.98 by addition of 1 g Instant Ocean® sea salt

191   per L and psu-offset. The natural pH of 8.1 after equilibration to the refrigerator's atmosphere

192   (at 2.5 °C and at atmospheric pressure), lowers to pH 8.05 at 2.5 °C at 150 bar (Culberson and

193   Pytkowicx, 1968). Five experiments, with 4 high-pressure chambers were carried out. The

194   Polar Surface (PSW) water corresponding experimental trial was running at -0.5 °C and 3 bar,

195   the experimental Atlantic Water (AW) trial at +2.5 °C and 65 bar, and three experimental

196   Deep Water trials were conducted at -1 °C and 100, 120 and 150 bar, respectively.

197   **2.4.2   Formaldehyde trial**

198   To study the effect of Formaldehyde treatment on cryogenic gypsum, the crystals were

199   subjected to a Formaldehyde solution of 4% in seawater, which is commonly used to preserve

200   biological samples. The stock solution consisted of 500 ml Formaldehyde concentration of

201   40%, 500 ml aqua dest. and 100 g hexamethylenetetramine, adjusted to a pH of 7.3-7.9.

202   Aliquots of the 20% stock solution were added to the four-fold volume of artificial Arctic

203   Ocean sea water to obtain a final concentration of 4%.

204   The Gypsum crystals were transferred into Falcon Tubes, and the 4% Formaldehyde solution

205   was added. The Falcon tubes were then either stored at 3 °C, or at room temperature. After

206   the experiments, the gypsum crystal-Formaldehyde suspension was washed with deionized

207   water over a 10 μm mesh using a wash bottle, and dried on gauze. As in all formaldehyde

208   trials all gypsum dissolved, no post-experimental weight was determined.

209

210   **2.5   Size-specific settling velocities of gypsum**

211

212   The size-specific sinking velocity of cryogenic gypsum was measured in a settling cylinder

213   (Ploug et al., 2008). The cylinder (30 cm high and 5 cm in diameter) was filled with filtered

214   seawater (salinity 32) and surrounded by a water jacket for thermal stabilization at 2 °C. The

215   settling cylinder was closed at both ends, only allowing insertion of a wide-bore pipette at the

216   top. Immediately before measurement, the gypsum was submerged into seawater with a

217   salinity of 32 and a temperature of 2 °C, and then transferred to the settling cylinder with a

218   wide-bore pipette. The gypsum crystals were allowed to sink out of the wide-bore pipette,

219   which was centered in the cylinder. The descent of the crystals was recorded by a Basler 4

220   MPixel Ethernet camera equipped with a 25 mm fixed focal lens (Edmund Optics). The

221   settling column was illuminated from the sides by a custom-made LED light source. The

222   camera recorded 7 images per second as the gypsum crystals sank through the settling

223   column. The measurements were only done with one camera, so a two-dimensional view. We

224   measured over a distance of ~5 cm after the crystals had reached terminal settling velocity

and at stable and constant temperature and salinity. The technical uncertainties of the setup were smaller that the uncertainties between two similar sized gypsum crystals, which had up to 1000 m/d uncertainties (see figure 6, with equivalent spherical diameters of ~1 mm). The setup was calibrated by recording a length scale before sinking velocity measurements. The size and settling of the individual gypsum crystals was determined with the image analysis software ImageJ. This was done by using the projected area of the crystals to calculate the equivalent spherical diameter and the distance traveled between the subsequent images to determine the sinking velocity of the individual crystals (Iversen et al., 2010)

2.6   Backtracking the sampled ice flows under which cryogenic gypsum was sampled

To determine sea ice drift trajectories of sampled sea ice we used a Lagrangian approach (IceTrack) that traces sea ice backward or forward in time using a combination of satellite-derived low resolution drift products. So far, IceTrack has been used in a number of publications to examine sea ice sources, pathways, thickness changes and atmospheric processes acting on the ice cover (Damm et al., 2018; Krumpen et al., 2016; Peeken et al., 2018). A detailed description is provided in Krumpen et al. (2019).

Sea ice motion information was provided by different institutions, obtained from different sensors, and for different time intervals. In this study we applied a combination of three different products: (i) motion estimates based on a combination of scatterometer and radiometer data provided by the Center for Satellite Exploitation and Research (CERSAT (Girard-Ardhuin and Ezraty, 2012), (ii) the OSI-405-c motion product from the Ocean and Sea Ice Satellite Application Facility (OSISAF (Lavergne, 2016), and (iii) Polar Pathfinder Daily Motion Vectors from the National Snow and Ice Data Center (NSIDC (Tschudi et al., 2016).

The tracking approach works as follows: An ice parcel is traced backward or forward in time on a daily basis. Tracking is stopped if a) ice hits the coastline or fast ice edge, or b) ice concentration at a specific location drops below 50% and we assume the ice to be formed or melted. The applied sea ice concentration product was provided by CERSAT and was based on 85 GHz SSM/I brightness temperatures, using the ARTIST Sea Ice (ASI) algorithm.

3   Results

3.1 Presence and distribution of cryogenic gypsum under the investigated ice-floes

Based on backtracking (Krumpen, 2018) and sea ice observations, the sampled ice-floes had an age of 1 to 3 years (Fig. 1B) and were originating from the Siberian Sea (station 32/80), the Laptev Sea (station 45), and were more locally grown in the Nansen Basin (station 66). Whereas the mean sea ice thickness at the ROV survey stations ranged between 94 and 156 cm, the mean sea ice thickness of the investigated ice-floes estimated by an ice-thickness sensor surveys (Katlein et al., 2018) was 1.90 m for station 32, 1.00 m for station 45, and 1.80 m for stations 66 and 80 (Fig. 1A, Table 1). Despite the different origins and thicknesses of sea ice, cryogenic gypsum crystals were found at all stations and in all depth layers sampled with the ROVnet (Figs. 1A, B, Tab. 1). At all stations and sampling depths the samples were dominated by cryogenic gypsum, with a proportional dry weight of >96.5% in the 5 m-sample at station 32, and with >99% in all other samples (Figs. 2, Figs. S2-S5). Other lithogenic particles, as often found in sea ice (Nürnberg et al., 1994), were essentially absent.

3.2 The morphology of cryogenic gypsum

The samples collected at station 32 were dominated by rounded, matte, solid cryogenic gypsum crystals with a mean length-width ratio of 1.40-1.76 (Tab. 2, S2). The proportional mass contribution of the smaller-sized crystals of the >30<63 μm size fraction increased with depth and outweighed the contribution of the >63 μm size fraction with 56.30%, and 66.28% for the 0 and 5 m water depth sample, respectively (Fig. 3). At 0 m, the mean length of the crystals was 68.46 μm in the >63 μm size fraction and 44.27 μm in the >30<63 μm fraction. At 5 m depth, crystal dimensions were similar, ranging at mean crystal lengths of 63.28 μm in the >63 μm, and 35.90 μm in the >30<63 μm size fraction, respectively.

At station 45, the crystals were mostly solid and for most part hyaline, rather than matte crystals as at station 32 (Figs. 2C-D, 6, S3). With decreasing weight proportion, the >63 μm size clearly dominated the 0, 5, and 10 m samples with 79.90, 73.39, and 66.14%, respectively. In the 0 m layer samples, mean crystal lengths were 114.18 μm in the >63 μm size fraction and 58.74 μm in the >30<63 μm size fraction (Tab. 2). At 5 m depth, we observed mean crystal lengths of 111 μm in the >63 μm size fractions, and 56.73 μm in the >30<63 μm fraction. The mean crystal lengths in the 10 m sample was 92.83 and 50.32 μm for the >63 and >30<63 μm size fraction, respectively. At station 45 the crystal length-width ratio varied between 1.37 and 1.98, measured in the >30<63 μm size fraction of the surface sample, and the >63 μm size fraction of the 10 m sample. The cryogenic gypsum crystals

289   retrieved from the melted ice core drilled at this station were solid and hyaline. In size and

290   shape they resembled the crystals of the 10 m layer at this station, with a mean crystal length

291   of 114.2 μm, mean width of 57.2 μm, and a length-width ratio of 2 (Fig. 4).

292   At station 66, the crystals from 0 m water depth were dominated by large, pencil-like, hyaline

293   and solid crystals with a mean crystal length of 1,355 μm and mean width of 415 μm in the

294   dominating >63 μm fraction (99.25% mass) (Fig. 2B, S4, Tab. 2). These crystals with an

295   average length-width ratio of 3.27 were found as isolated crystals, but very often also as inter-

296   grown crystal rosettes with two to more than 10 individual crystals involved (Fig. S4; Tab. 2).

297   The >30<63 μm size fraction (0.75% mass) was dominated by matte, whitish, rounded

298   gypsum particles and tiny gypsum needles with a mean crystal length of 56.67 μm (Fig. S4,

299   Tab. 2.). As at the other stations the weight proportion of the >63 μm size fraction

300   significantly decreased from 99.25 in the 0 m, to 75.23 at 5 m, and 61.18% in the 10 m

301   sample (Fig. 2). The size of cryogenic gypsum crystals collected from the 5 and 10 m layers

302   was significantly smaller and predominantly composed of isolated small hyaline and euhedral

303   gypsum needles. The length-width ratio ranged between 5.60 (5 m) and 4.37 (10 m) (Figs.

304   2A, S4, Tab. 2). In the 5 m layer sample, the mean crystal length was 411.42 μm in the >63

305   μm size fraction, and 62.03 μm in the >30<63 μm size fraction. The 10 m samples showed a

306   mean crystal length of 101.40 μm in the >63, and 30.71 μm in the >30<63 μm size fraction

307   (Tab. 2).

308   In the 10 m layer sample of station 80, large tabular gypsum crystals measuring up to 1 cm in

309   length (mean length: 3,078 μm, mean width: 1,830 μm) dominated the >63 μm size fraction.

310   Their average length-width ratio was 1.7. This size fraction contributed 89.1% of the gypsum

311   mass (Figs. 5, S5, Tab. 2). The >30<63 μm size fraction was composed of fragments of these

312   large crystals and few small gypsum needles. These often intergrown columnar crystals

313   looked bladed, for most part also dented and with numerous cracks. Their mean length was

314   71.8 μm. The ice core retrieved from this station was very porous and broke into pieces of 9

315   to 11 cm. Cryogenic gypsum was retrieved from all these ice core sections and revealed a

316   dominance of extraordinary large crystals (Figs. 5, S5), resembling the ROVnet samples from

317   this station. The largest cryogenic gypsum crystals >6,000 μm (mean crystal length: 2,821

318   μm, mean width: 1,689 m) were retrieved from the top-most 8 cm ice core section, whereas,

319   the maximum crystal size gradually decreased downcore (Fig. S5). The crystals themselves

320   lacked sharp corners, and the large crystals had cavities inside, indicating an advanced stage

321   of dissolution (Figs. 5C-D; S5).

322

3.3   Dissolution experiments

3.3.1   Experiments to simulate cryogenic gypsum dissolution within the Arctic water column

Our study area was characterized by the presence of three main water masses (Nikolopoulos et al., 2018; Rudels, 2015): 1) The Polar Surface Water (PSW) including the halocline, with a variable mean salinity of 32 and a temperature range of -1.8 to 0.0 °C, extended from the surface to maximum 100 m water depth (Nikolopoulos et al., 2018). 2) The Atlantic Water (AW) with a mean salinity of 34.4 to 34.7 and variable temperature of 0.0 to 4.7 °C in the study area extended from below the PSW to 600-800 m water depth (Nikolopoulos et al., 2018). 3) The Eurasian Arctic Deep Water (EADW) fills the deep Eurasian Basin below the AW with a temperature range of <0 to -0.94 °C and a salinity of about 34.9 (Nikolopoulos et al., 2018).

The dissolution experiments carried out to simulate dissolution in the PSW were set to 3 bar, -0.5 °C. Over the 24 hours lasting PSW-simulating dissolution experiment, about 6% of the gypsum dissolved (Figs. 6, S6A, Tab. 3). In the AW experiment, the combination of positive temperatures (2.5 °C) and a pressure of 65 bar impacted the dissolution on the cryogenic gypsum crystals more than in any other seawater trial. More than 80% of the cryogenic gypsum crystals dissolved during the 24-hours experiment (Figs. 6, S6B, Tab. 3). The EADW-simulating dissolution experiments set to a temperature of -0.5 °C showed a progressive cryogenic gypsum dissolution of 26, 58, and 62% with increasing pressure for the 100, 120 and 150 bar experiments, respectively (Figs. 6, S7, Tab. 3). Moreover, as dissolution mainly affects the crystal's surface, smaller gypsums crystals and those with increased surface roughness (S8C-D) were preferentially impacted by dissolution, whereas larger and solid crystals with smooth surface showed the lowest dissolution (S8A-B).

3.3.2   Experiments to simulate cryogenic gypsum dissolution within Formaldehyde-treated biological samples

In the Formaldehyde experiments we exposed our set of cryogenic gypsum crystals to a Formaldehyde solution of 4%, which is commonly used to store pelagic samples from the

351 Polar Oceans (Edler, 1979). Irrespective of the temperature at which the sample was stored,

352 all gypsum dissolved within 24 hours.

353 **3.4 Sinking velocities of gypsum crystals**

354

355 The sinking velocity (*SV*) of the gypsum crystals increased with crystal size (Fig. 7). Small

356 crystals with an equivalent spherical diameter (*ESD*) of 200 μm sank with 300 m d^{-1} while

357 large gypsum crystals with ESDs of 2,000 to 2,500 μm sank with velocities of 5,000 to 7,000

358 m d^{-1}. The size to settling relationship was best described by a power function (SV = 4239.9

359 ESD$^{0.839}$, R^2 = 0.84).

360

361 **4 Discussion**

362

363 **4.1 Distribution and morphology of cryogenic gypsum crystals**

364

365 This study shows for the first time the wide-spread presence of cryogenic gypsum under melting

366 Arctic sea ice of different origin. At all stations cryogenic gypsum dominated the sample

367 fraction of particles >30 μm in Eurasian Basin surface waters, indicating a continuous cryogenic

368 gypsum flux from melting sea ice over a period of six weeks.

369 When designing the ROVnet for cryogenic gypsum sampling, we opted for the coarser >30 μm

370 mesh to prohibit an overflow of the sampling container when running into a phytoplankton

371 bloom. However, as Geilfus et al. (Geilfus et al., 2013) had observed gypsum crystals as small

372 as 10 μm, we probably lost an unknown proportion of smaller gypsum crystals by the chosen

373 sampling strategy. The gypsum crystals described from sea ice so far retrieved from only 3-

374 days-old experimental and 30 cm thick natural sea ice off Greenland were small (crystal length

375 max. 100 μm), planar euhedral gypsum crystals often intergrown or as rosettes (Geilfus et al.,

376 2013). Similar, but larger (crystal length up to 1 mm), gypsum crystals were observed within

377 *Phaeocystis* aggregates collected in the region of the present study (Wollenburg et al., 2018a).

378 However, here we show that gypsum crystals exhibit a strong variability in size and

379 morphology. Particularly large crystals were characterised by more complex shapes (Fig. 2, 5,

380 S3-4) and increased surface roughness (Figs. S8C-D), compared to the small planar euhedral

381 (Fig. 2A) and more spherical crystals (Fig. S8A-B). Euhedral crystal needles larger but

382 otherwise similar to those described by Geilfus et al. (2013) and Wollenburg et al. (2018a)

383 dominated the >63 μm fraction collected at 5 and 10 m depths at station 66, and smaller crystals

384 contributed especially to the >30<63 μm size fraction of the station's subsurface samples.

385 As cryogenic gypsum forms in sea ice brine pockets or channels, the size and morphology

386 especially of large crystals is likely determined by sea ice texture and porosity during gypsum

387 precipitation. Pursuing this hypothesis, the large and intergrown crystals collected from the

388 0 m layer at station 66, and the 10 m layer and ice-core at station 80, formed in highly

389 branched granular sea ice (Lieb-Lappen et al., 2017; Weissenberger et al., 1992). In contrast,

390 the small cryogenic gypsum needles reported by Geilfus et al. (2013) and Wollenburg et al. (

391 2018a), may have preferentially formed in columnar sea ice. Even sampling the same ice-floe

392 (station 32 and 80), the appearance of the crystals changed. Possibly, a widening of the brine

393 channels during the elapsed time (6 weeks) allowed a release of larger crystals at station 80

394 when compared to station 32. However, crystal growth during this elapsed period or lateral

395 advection of large crystals cannot be excluded. Thus, detailed texture analyses on sea ice

396 cores prior to sampling are needed to validate or reject hypotheses on a link between sea ice

397 porosity and cryogenic gypsum crystal size and morphology and should be considered in

398 future studies.

399 The sea ice microstructure dictating the formation of gypsum crystals in the brine matrix

400 likely varied among ice-floes due to different ages, origins and drift trajectories (Fig. 1B). For

401 example, station 66 was the only station where the sea ice likely formed over the central

402 Nansen Basin only months before our study (Fig. 1B). The surface sample of station 66 had

403 large intergrown hyaline star-shaped gypsum crystals that were observed at no other station.

404 They also showed a considerably higher length-width ratio than crystals from second-year ice

405 of stations 32/80 and 45 (Fig. 1B; Fig. 2). Accordingly, a close relationship between local sea

406 ice properties and gypsum crystal morphology in the underlying water was evident from the

407 comparison of gypsum crystals collected with the ROVnet with those retrieved from ice cores

408 collected at two stations. The ice-core samples revealed cryogenic gypsum crystals that

409 basically resembled the crystal morphologies collected from the water column at the same

410 stations, indicating that the gypsum morphologies observed in the water column likely reflect

411 the gypsum precipitation conditions and brine-channel structure of local ice-floes. The current

412 understanding of mineral precipitation in supersaturated brines relies on ice-core analyses, sea

413 ice brine- and experimental studies, and on mathematical modelling of the temperature

414 window in which each mineral is likely to form (Butler et al., 2017; Marion et al., 2010).

415 There are still many uncertainties regarding the precipitation and dissolution of gypsum

416   within natural sea ice and during ice-core storage. Although the FREZCHEM model and

417   Gitterman Pathway predict gypsum precipitation under defined conditions, only Geilfus et al.

418   (Geilfus et al., 2013) and Butler et al. (Butler et al., 2017) succeeded in retrieving gypsum

419   under such conditions, whereas others failed (Butler and Kennedy, 2015). According to the

420   FREZCHEM model, cryogenic gypsum precipitates at temperatures of -6.2 to -8.5 °C and at

421   temperatures <-18 °C (Geilfus et al., 2013; Wollenburg et al., 2018a). Accordingly, a storage

422   temperature of -20 °C would allow the post-coring precipitation of gypsum from contained

423   brines. However, in field and experimental studies cryogenic gypsum was so far only

424   observed to precipitate in the -6.2 to -8.5 °C temperature window, even when treatments were

425   conducted below -20 °C (Butler et al., 2017; Geilfus et al., 2013). Furthermore, the observed

426   signs of dissolution on the large cryogenic gypsum crystals from the ice-core when compared

427   to the sharp-edged crystals retrieved from the water column at station 80 indicate that

428   significant new precipitation of gypsum during storage did not occur, rather the opposite.

429   Apart from the growing conditions of gypsum crystals within sea ice, the size spectrum of

430   crystals retrieved from different depths in the water column likely was essentially altered by

431   the size-dependent sinking velocity of the crystals. Because the sinking velocity of large

432   cryogenic gypsum crystals is high the chance to catch large crystals with horizontal transects

433   directly under the ice should be lower compared to small crystals (Fig. 7A). Accordingly,

434   significant amounts of large cryogenic gypsum crystals were mainly sampled from the 0 m

435   layer where they could be scraped off the underside of the ice (see station 66, Tab. 2). In

436   contrast, smaller cryogenic gypsum crystals sink at lower velocities (Fig. 7A). Hence, the

437   large quantity of small-sized crystals retrieved in the deeper layers of station 66, and all layers

438   of station 32 and 45 likely were influenced by the accumulated gypsum release in this size-

439   fraction, whereas the rarer large crystals indicated the momentary release at these stations.

440   The extremely large crystals sampled at station 80 at 10 m depth probably indicated an on-

441   going flux event during rapid melting. According to our dissolution experiments, gypsum

442   dissolution within Arctic surface waters should only have a minor impact on the size

443   distribution of cryogenic gypsum crystals within the surface water. Besides vertical flux,

444   advection of gypsum crystals with surface currents may also have influenced the size-

445   distribution of gypsum crystals sampled in the water column.

446

447   **4.2   Reasons why cryogenic gypsum was rarely observed in past studies**

448

449   The small temperature range of the -6.2 to -8.5 °C window, which is also the only gypsum

450   precipitation temperature spectrum applicable in the Arctic Ocean, has been considered one

451   reason why gypsum was not detected in other studies (Butler and Kennedy, 2015; Wollenburg

452   et al., 2018a). Furthermore, the kinetics of gypsum precipitation was considered as too slow

453   for detection during experimental studies, and the amount of gypsum hard to verify versus

454   other sea ice precipitates that are quantitatively much more abundant, leading the focus

455   towards other sea ice precipitates (Butler and Kennedy, 2015; Geilfus et al., 2013). Although

456   cryogenic mirabilite and hydrohalite are three and twenty-two times more abundant than

457   gypsum, respectively (Butler and Kennedy, 2015), gypsum is the only sea ice precipitate that

458   survives for one to several days within the Arctic water column. Cryogenic gypsum

459   dissolution increases with increasing hydrostatic pressure and increasing temperatures (Fig.

460   6). However, well-preserved cryogenic gypsum crystals were retrieved from algae aggregates

461   collected from 2,146 m water depth, suggesting that either the transport from the surface to

462   this depth was very rapid or that dissolution was decreased and/or prevented once gypsum

463   crystals were included within the matrix of organosulfur compound-rich aggregates

464   (Wollenburg et al., 2018a). Yet, as seawater is usually undersaturated with respect to gypsum

465   (Briskin and Schreiber, 1978a; Briskin and Schreiber, 1978b) and is shown by our dissolution

466   experiments, disaggregation of organic aggregates would expose the gypsum to the seawater

467   and dissolve any crystals making it to the deep ocean or seafloor likely within a few days. The

468   same dissolution would occur within the sampling cups of sediment traps, explaining why

469   gypsum has not been observed in those type of samples.

470   Our dissolution experiments showed that cryogenic gypsum can persist long enough in the

471   cold polar surface water to be collected in measurable concentrations. The missing evidence

472   of gypsum from past studies was likely due to the quick dissolution of gypsum crystals at

473   higher temperatures and pressure dependence of dissolution kinetics, impeding the discovery

474   of gypsum in sediment trap samples and on the sea-floor. In addition, Formaldehyde

475   preservation leads to the immediate dissolution of gypsum, destroying any evidence of

476   cryogenic gypsum in all kinds of biological samples including water column and net samples.

477   Based on our experience with the PS106 expedition samples and the experiments presented

478   here, we propose a standardized procedure for gypsum sampling in the field. This procedure

479   is part of the standard operating protocol for gypsum samplind on the MOSAIC expedition

480   (S 9).

481

482   **4.3   Potential of cryogenic gypsum as a ballast of algae blooms**

483

484 We found less than 6% dissolution of individual crystals in Polar Surface Water (PSW) per

485 day. Thus, at depths immediately below the fluorescence maximum where a significant part

486 of organic aggregates are formed (Iversen et al. 2010), the gypsum scavenging and ballasting

487 of aggregates (Turner, 2015) is little affected by gypsum dissolution (Olli et al., 2007) (Fig. 6,

488 Tab. 3). Incorporation of dense minerals into settling organic aggregates will increase their

489 density and, therefore, the size-specific sinking velocities of the aggregates (Iversen and

490 Ploug, 2010; Iversen and Robert, 2015; van der Jagt et al., 2018). The high sinking velocity of

491 large gypsum crystals >1 mm (5,000-7,000 m d^{-1} (Fig. 7A)) could create strong hydrodynamic

492 shear that might cause disaggregation of fragile algae aggregates (Olli et al., 2007). However,

493 smaller gypsum crystals have been observed inside *Phaeocystis* aggregates collected at depths

494 below 2000 m (Wollenburg et al. 2018a). This shows that cryogenic gypsum is incorporated

495 into organic aggregates and supports that gypsum can be an important ballast mineral of

496 organic aggregates.

497 As chlorophyll concentrations in the surface water were mostly low (< 1 mg m^{-3}, H.F.

498 unpublished data), a massive gypsum-mediated export of phytoplankton was unlikely during

499 expedition PS106. However, especially at the ice floe of station 32/80, we observed a high

500 coverage of the ice underside by the filamentous algae *Melosira arctica*, and gypsum crystals

501 were found in *M. arctica* filaments collected nearby (Fig. 8) as well as at station 45 (Fig. 2D).

502 This indicates a potential for rapid *M. arctica* downfall mediated by cryogenic gypsum, as

503 soon as the algal filaments were released from the melting sea ice. Hence, ballasting by

504 cryogenic gypsum may also have contributed to the mass export of *Melosira arctica*

505 aggregates observed in 2012 (Boetius et al. 2013).

506

507

508

509 **5   Conclusions**

510 This study shows for the first time that gypsum released to the water at the onset of melt

511 season in the Arctic Ocean causes a constant flux of gypsum over wide spread areas and over

512 a long period of time (> six weeks). The morphological diversity of gypsum crystals retrieved

513 from Arctic surface waters and ice-cores indicated a complex variety of precipitation and

514 release processes as well as modifications during sea ice formation, the melt phase, and in the

515 water column. In the fresh and cold Polar surface water, gypsum crystals persist long enough

516   to act as an effective ballast on organic matter, such as phytoplankton filaments and marine

517   snow.

518

519   **References:**

520   Arrigo, K. R., Perovich, D. K., Pickart, R. S., Brown, Z. W., van Dijken, G. L., Lowry, K. E., Mills,
521   M. M., Palmer, M. A., Balch, W. M., Bahr, F., Bates, N. R., Benitez-Nelson, C., Bowler, B.,
522   Brownlee, E., Ehn, J. K., Frey, K. E., Garley, R., Laney, S. R., Lubelczyk, L., Mathis, J., Matsuoka,
523   A., Mitchell, B. G., Moore, G. W. K., Ortega-Retuerta, E., Pal, S., Polashenski, C. M., Reynolds,
524   R. A., Schieber, B., Sosik, H. M., Stephens, M., and Swift, J. H.: Massive Phytoplankton
525   Blooms Under Arctic Sea Ice, Science, 336, 1408, 2012.

526

527   Arrigo, K. R., Perovich, D. K., Pickart, R. S., Brown, Z. W., van Dijken, G. L., Lowry, K. E., Mills,
528   M. M., Palmer, M. A., Balch, W. M., Bates, N. R., Benitez-Nelson, C. R., Brownlee, E., Frey, K.
529   E., Laney, S. R., Mathis, J., Matsuoka, A., Greg Mitchell, B., Moore, G. W. K., Reynolds, R. A.,
530   Sosik, H. M., and Swift, J. H.: Phytoplankton blooms beneath the sea ice in the Chukchi sea,
531   Deep Sea Research Part II: Topical Studies in Oceanography, 105, 1-16, 2014.

532

533   Assmy, P., Fernández-Méndez, M., Duarte, P., Meyer, A., Randelhoff, A., Mundy, C. J., Olsen,
534   L. M., Kauko, H. M., Bailey, A., Chierici, M., Cohen, L., Doulgeris, A. P., Ehn, J. K., Fransson, A.,
535   Gerland, S., Hop, H., Hudson, S. R., Hughes, N., Itkin, P., Johnsen, G., King, J. A., Koch, B. P.,
536   Koenig, Z., Kwasniewski, S., Laney, S. R., Nicolaus, M., Pavlov, A. K., Polashenski, C. M.,
537   Provost, C., Rösel, A., Sandbu, M., Spreen, G., Smedsrud, L. H., Sundfjord, A., Taskjelle, T.,
538   Tatarek, A., Wiktor, J., Wagner, P. M., Wold, A., Steen, H., and Granskog, M. A.: Leads in
539   Arctic pack ice enable early phytoplankton blooms below snow-covered sea ice, Scientific
540   Reports, 7, 40850, 2017.

541

542   Briskin, M. and Schreiber, B. C.: Authigenic gypsum in marine sediments, Marine Geology,
543   28, 37-49, 1978.

544

545   Butler, B.: Mineral dynamics in sea ice brines, PhD, Bangor, 184 pp., 2016.

546

547   Butler, B. M. and Kennedy, H.: An investigation of mineral dynamics in frozen seawater
548   brines by direct measurement with synchrotron X-ray powder diffraction, Journal of
549   Geophysical Research: Oceans, 120, 5686-5697, 2015.

550

551   Butler, B. M., Papadimitriou, S., Day, S. J., and Kennedy, H.: Gypsum and hydrohalite
552   dynamics in sea ice brines, Geochimica et Cosmochimica Acta, 213, 17-34, 2017.

553

554   Culberson, C. and Pytkowicx, R. M.: Effect of pressure on carbonic acid, boric acid, and the
555   pH in seawater, Limnology and Oceanography, 13, 403-417, 1968.

556

557   Damm, E., Bauch, D., Krumpen, T., Rabe, B., Korhonen, M., Vinogradova, E., and Uhlig, C.:
558   The Transpolar Drift conveys methane from the Siberian Shelf to the central Arctic Ocean,
559   Scientific Reports, 8, 4515, 2018.

560

561 Docquier, D., Massonnet, F., Barthélemy, A., Tandon, N. F., Lecomte, O., and Fichefet, T.:
562 Relationships between Arctic sea ice drift and strength modelled by NEMO-LIM3.6, The
563 Cryosphere, 11, 2829-2846, 2017.
564
565 Edler, L.: Recommendations on Methods for Marine Biological Studies in the Baltic Sea:
566 Phytoplankton and chlorophyll, Department of Marine Botany, University of Lund, 1979.
567
568 Flores, H. E., J.; Lange, B.; Sulanke, E.; Niehoff, B.; Hildebrandt, N.; Doble, M.; Schaafsma, F.;
569 Meijboom, A.; Fey, B.; Kühn, S.; Bravo-Rebolledo; E.; Dorssen, M. van; Grandinger, R.;
570 Hasset, B.; Kunisch, E.; Kohlbach, D.; Graeve, M.; Franeker, J. A. van; Gradinger, Bluhm, B.:
571 Under-ice fauna, zooplankton and endotherms. In: The Expeditions PS106/1 and 2 of the
572 Research Vessel Polarstern to the Arctic Ocean in 2017, Macke, A. F., H. (Ed.), Reports on
573 polar and marine research, 2018.
574
575 Geilfus, N. X., Galley, R. J., Cooper, M., Halden, N., Hare, A., Wang, F., Søgaard, D. H., and
576 Rysgaard, S.: Gypsum crystals observed in experimental and natural sea ice, Geophysical
577 Research Letters, 40, 6362-6367, 2013.
578
579 Girard-Ardhuin, F. and Ezraty, R.: Enhanced Arctic Sea Ice Drift Estimation Merging
580 Radiometer and Scatterometer Data, IEEE Transactions on Geoscience and Remote Sensing,
581 50, 2639-2648, 2012.
582
583 Golden, K. M., Ackley, S. F., and Lytle, V. I.: The Percolation Phase Transition in Sea Ice,
584 Science, 282, 2238, 1998.
585
586 Iversen, M., Nowald, N., Ploug, H., A. Jackson, G., and Fischer, G.: High resolution profiles of
587 vertical particulate organic matter export off Cape Blanc, Mauritania: Degradation processes
588 and ballasting effects, Deep Sea Research Part I Oceanographic Research Papers, 57, 771-
589 784, 2010.
590
591 Iversen, M. H. and Ploug, H.: Ballast minerals and the sinking carbon flux in the ocean:
592 carbon-specific respiration rates and sinking velocity of marine snow aggregates,
593 Biogeosciences, 7, 2613-2624, 2010.
594
595 Iversen, M. H. and Robert, M. L.: Ballasting effects of smectite on aggregate formation and
596 export from a natural plankton community, Marine Chemistry, 175, 18-27, 2015.
597
598 Katlein, C., Arndt, S., Nicolaus, M., Perovich, D. K., Jakuba, M. V., Suman, S., Elliott, S.,
599 Whitcomb, L. L., McFarland, C. J., Gerdes, R., Boetius, A., and German, C. R.: Influence of ice
600 thickness and surface properties on light transmission through Arctic sea ice, Journal of
601 Geophysical Research: Oceans, 120, 5932-5944, 2015.
602
603 Katlein, C., Nicolaus, M., Sommerfeld, A., Copalorado, V., Tiemann, L., Zanatta, M., Schulz,
604 H., and Lange, B.: Sea Ice Physics. In: The Expeditions PS106/1 and 2 of the research vessel
605 Polarstern in the Arctic Ocean in 2017, Macke, A. F., H. (Ed.), Berichte zur Polarforschung
606 Bremerhaven, 2018.
607

608 Katlein, C., Schiller, M., Belter, H. J., Coppolaro, V., Wenslandt, D., and Nicolaus, M.: A New
609 Remotely Operated Sensor Platform for Interdisciplinary Observations under Sea Ice,
610 Frontiers in Marine Science, 4, 281, 2017.
611
612 Krumpen, T.: AWI ICETrack - Antarctic and Arctic Sea Ice Monitoring and Tracking Tool
613 Alfred-Wegener-Institut Hemholtz-Zentrum für Polar- und Meeresforschung, Bremerhaven,
614 Germany, 2018.
615
616 Krumpen, T., Belter, H. J., Boetius, A., Damm, E., Haas, C., Hendricks, S., Nicolaus, M., Nöthig,
617 E.-M., Paul, S., Peeken, I., Ricker, R., and Stein, R.: Arctic warming interrupts the Transpolar
618 Drift and affects long-range transport of sea ice and ice-rafted matter, Scientific Reports, 9,
619 5459, 2019.
620
621 Krumpen, T., Gerdes, R., Haas, C., Hendricks, S., Herber, A., Selyuzhenok, V., Smedsrud, L.,
622 and Spreen, G.: Recent summer sea ice thickness surveys in Fram Strait and associated ice
623 volume fluxes, The Cryosphere, 10, 523-534, 2016.
624
625 Kwok, R.: Arctic sea ice thickness, volume, and multiyear ice coverage: losses and coupled
626 variability (1958–2018), Environmental Research Letters, 13, 105005, 2018.
627
628 Kwok, R. and Rothrock, D. A.: Decline in Arctic sea ice thickness from submarine and ICESat
629 records: 1958‚Äì2008, Geophys. Res. Lett., 36, 2009.
630
631 Lavergne, T.: Validation and Monitoring of the OSI SAF Low Resolution Sea Ice Drift Product
632 (v5), 2016.
633
634 Lieb-Lappen, R. M., Golden, E. J., and Obbard, R. W.: Metrics for interpreting the
635 microstructure of sea ice using X-ray micro-computed tomography, Cold Regions Science and
636 Technology, 138, 24-35, 2017.
637
638 Marion, G. M., Mironenko, M. V., and Roberts, M. W.: FREZCHEM: A geochemical model for
639 cold aqueous solutions, Computers & Geosciences, 36, 10-15, 2010.
640
641 Nicolaus, M., Arndt, S., Katlein, C., Maslanik, J., and Hendricks, S.: Correction to "Changes in
642 Arctic sea ice result in increasing light transmittance and absorption", Geophysical Research
643 Letters, 40, 2699-2700, 2013.
644
645 Nicolaus, M., Katlein, C., Maslanik, J., and Hendricks, S.: Changes in Arctic sea ice result in
646 increasing light transmittance and absorption, Geophysical Research Letters, 39, 2012.
647
648 Nikolopoulos, A., Heuzé, C., Linders, T., Andrée, E., and Sahlin, S.: Physical Oceanography. In:
649 The Expeditions PS106/1 and 2 of the Research Vessel POLARSTERN to the Arctic Ocean in
650 2017, Macke, A. and Flores, H. (Eds.), Reports on Polar and Marine Research, Alfred-
651 Wegener Institute Helmholtz Centre for Polar and marine research, Bremerhaven, 2018.
652
653 Nürnberg, D., Wollenburg, I., Dethleff, D., Eicken, H., Kassens, H., Letzig, T., Reimnitz, E., and
654 Thiede, J.: Sediments in Arctic sea ice: Implications for entrainment, transport and release,
655 Marine Geology, 119, 185-214, 1994.

656

657　Olli, K., Wassmann, P., Reigstad, M., Ratkova, T. N., Arashkevich, E., Pasternak, A., Matrai, P.
658　A., Knulst, J., Tranvik, L., Klais, R., and Jacobsen, A.: The fate of production in the central
659　Arctic Ocean - top-down regulation by zooplankton expatriates?, Progress In Oceanography,
660　72, 84-113, 2007.

661

662　Peeken, I., Primpke, S., Beyer, B., Gütermann, J., Katlein, C., Krumpen, T., Bergmann, M.,
663　Hehemann, L., and Gerdts, G.: Arctic sea ice is an important temporal sink and means of
664　transport for microplastic, Nature Communications, 9, 1505, 2018.

665

666　Peeken, I. C., G.; Flores, H.; Ehrlich, J.; Lange, B.; Schaafsma, F., Gradinger, R.; Hassett, B.;
667　Kunisch, E.; Damm, E.; Verdugo, J.; Kohlbach, D.; Graeve, M.; Bluhm, B.: Sea ice biology and
668　biogeochemistry. In: The Expeditions PS106/1 and 2 of the Research Vessel Polarstern to the
669　Arctic Ocean in 2017, Macke, A. F., H. (Ed.), 719, Reports of polar and marine research, 2018.

670

671　Ploug, H., Iversen, M. H., Koski, M., and Buitenhuis, E. T.: Production, oxygen respiration
672　rates, and sinking velocity of copepod fecal pellets: Direct measurements of ballasting by
673　opal and calcite, Limnology and Oceanography, 53, 469-476, 2008.

674

675　Rudels, B.: Arctic Ocean circulation, processes and water masses: A description of
676　observations and ideas with focus on the period prior to the International Polar Year 2007–
677　2009, Progress in Oceanography, 132, 22-67, 2015.

678

679　Schneider, C. A., Rasband, W. S., and Eliceiri, K. W.: NIH Image to ImageJ: 25 years of image
680　analysis, Nature Methods, 9, 671, 2012.

681

682　Smedsrud, L. H., Halvorsen, M. H., Stroeve, J. C., Zhang, R., and Kloster, K.: Fram Strait sea ice
683　export variability and September Arctic sea ice extent over the last 80 years, The Cryosphere,
684　11, 65-79, 2017.

685

686　Strunz, H. and Nickel, E. H.: Strunz Mineralogical Tables. Chemical-structural Mineral
687　Classification System, Schweizerbart'sche Verlagsbuchhandlung (Nägele u. Obermiller),
688　Stuttgart, 2001.

689

690　Tschudi, S., Fowler, C., Maslanik, J., Stewart, J., and Stewart, W.: Polar Pathfinder Daily 25 km
691　EASE-Grid Sea Ice Motion Vectors. In: Technical report, NASA National Snow and Ice Data
692　Center Distributed Active Archive Center, Boulder, Colorado USA 2016.

693

694　Turner, J. T.: Zooplankton fecal pellets, marine snow, phytodetritus and the ocean's
695　biological pump, Progress in Oceanography, 130, 205-248, 2015.

696

697　van der Jagt, H., Friese, C., Stuut, J.-B. W., Fischer, G., and Iversen, M. H.: The ballasting
698　effect of Saharan dust deposition on aggregate dynamics and carbon export: Aggregation,
699　settling, and scavenging potential of marine snow, Limnology and Oceanography, 63, 1386-
700　1394, 2018.

701

702 Weissenberger, J., Dieckmann, G., Gradinger, R., and Spindler, M.: Sea ice: A cast technique
703 to examine and analyze brine pockets and channel structure, Limnology and Oceanography,
704 37, 179-183, 1992.
705

706 Wollenburg, J. E., Katlein, C., Nehrke, G., Nöthig, E. M., Matthiessen, J., Wolf- Gladrow, D. A.,
707 Nikolopoulos, A., Gázquez-Sanchez, F., Rossmann, L., Assmy, P., Babin, M., Bruyant, F.,
708 Beaulieu, M., Dybwad, C., and Peeken, I.: Ballasting by cryogenic gypsum enhances carbon
709 export in a Phaeocystis under-ice bloom, Scientific Reports, 8, 7703, 2018a.
710

711 Wollenburg, J. E., Zittier, Z. M. C., and Bijma, J.: Insight into deep-sea life – Cibicidoides
712 pachyderma substrate and pH-dependent behaviour following disturbance, Deep Sea
713 Research Part I: Oceanographic Research Papers, 138, 34-45, 2018b.
714

715

716

717   **Table captions:**

718

719   Tab. 1: Properties of sea ice stations and characteristics of ROVnet profiles.

Cruise Site	Date	Latitude (Deg N)	Longitude (Deg E)	Ocean depth (m)	Sampling depth	Water temp. (°C)	Salinity	Mean ice thickness (m)	Filtered water volume (m³)
PS106.1 Stat. 32	2017-06-15	81.73	10.86	1608	under-ice	-1.94	34.27	1.90	2.2
					5 m	n.a	n.a.	1.90	3.9
PS106.2 Stat. 45	2017-06-25	78.10	30.47	233	under-ice	-1.52	33.84	1.00	2.3
					5 m	-1.47	34.11	1.00	4.5
					10 m	-1.68	34.29	1.00	2.5
PS106.2 Stat. 66	2017-07-02	81.66	32.34	1506	under-ice	-1.67	33.18	1.80	3.1
					5 m	-1.71	33.76	1.80	2.7
					10 m	-1.73	33.78	1.80	3.1
PS106.2 Stat. 80	2017-07-12	81.37	17.13	1010	10 m	-1.37	32.87	1.80	1.7

720
721

722   Tab. 2: Size measurements and percentage of mass contribution of gypsum crystals from the

723   >63 μm size fraction and the >30 < 63 μm size fraction

Cruise, Site, mean water depth of the catch	>63 µm fraction			>30<63 µm fraction			>63 µm fraction weight%	>30<63 µm fraction weight%
	Mean length µm	Mean width µm	length/ width ratio	Mean length µm	Mean width µm	length/ width ratio		
PS106.1, Stat. 32, 0 m	68.46	44.27	1.55	50.64	35.03	1.45	43.70	56.30
PS106.1, Stat. 32, 5 m	63.28	35.90	1.76	49.91	35.57	1.40	33.72	66.28
PS106.1, Stat. 32, mean (0-5 m)	65.87	40.09	1.64	50.28	35.30	1.42	38.71	61.29
PS106.2, Stat. 45, 0 m	114.18	65.93	1.73	58.74	42.84	1.37	79.90	20.10
PS106.2, Stat. 45, 5 m	110.98	64.84	1.71	56.73	38.89	1.46	73.39	26.61
PS106.2, Stat. 45 , 10 m	92.83	46.81	1.98	50.32	29.98	1.68	66.14	33.86
PS106.2, Stat. 45 , mean (0-10 m)	85.49	44.45	1.92	77.93	24.28	3.21	73.14	26.86
PS106.2, Stat. 66, 0 m	1355.38	415.10	3.27	56.67	25.63	2.21	99.25	0.75
PS106.2, Stat. 66, 5 m	411.42	73.45	5.60	62.03	12.20	5.08	75.23	24.77
PS106.2, Stat. 66, 10 m	101.40	23.19	4.37	30.71	5.79	5.30	61.18	38.82
PS106.2, Stat. 66, mean (0-10 m)	599.17	164.78	3.64	59.96	12.61	4.76	58.16	41.84
PS106.2, Stat. 80, 10 m	3078.44	1830.00	1.68	71.78	30.76	2.33	89.05	10.95

724

725

726

727   Tab. 3: Dissolution experiments on cryogenic gypsum crystals. 'Water mass' simulating

728   experiments with 34.9‰ sterile filtered seawater. Each experiment was conducted in parallel

729   in 3-4 separate pressure chambers.

Chamber (no.)/Water mass	Dissolution in weight%				
	PSW	AW	EADW (1)	EADW (2)	EADW (3)
1	11.34	76.22	47.52	57.08	74.92
2	1.33	86.23	26.09	71.03	53.77
3	8.29	82.93	21.05	47.15	57.43
4	2.99	78.57	10.91	58.56	
Mean	**5.99**	**80.77**	**26.39**	**58.34**	**62.04**

730

731

Figure captions:
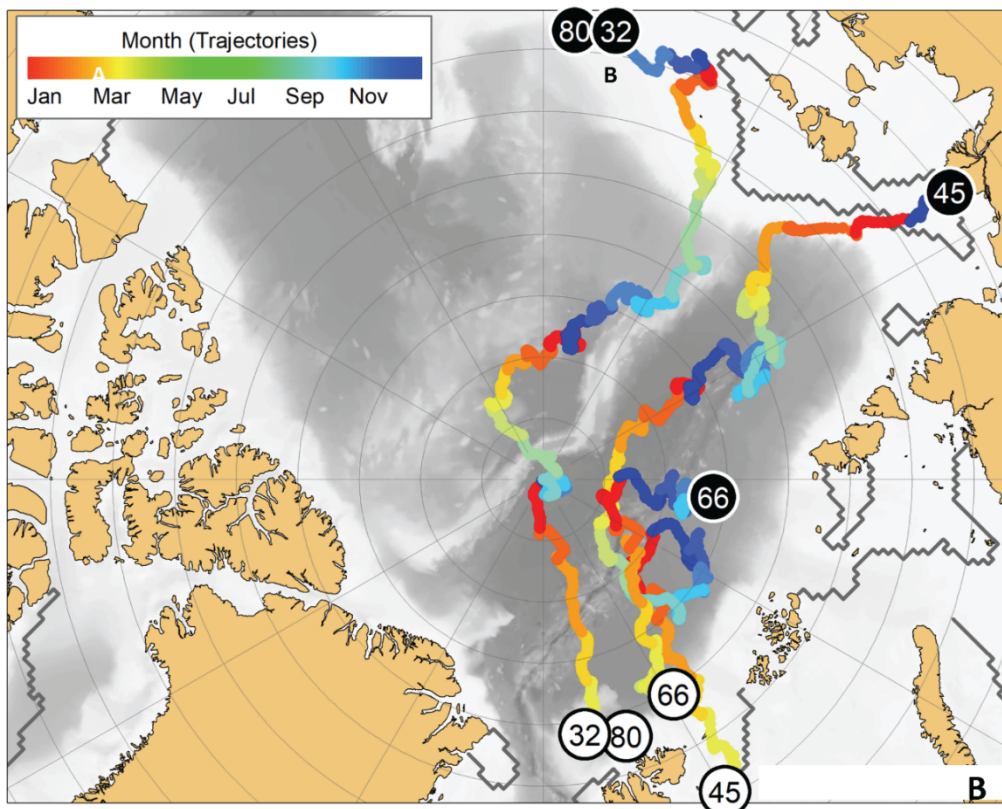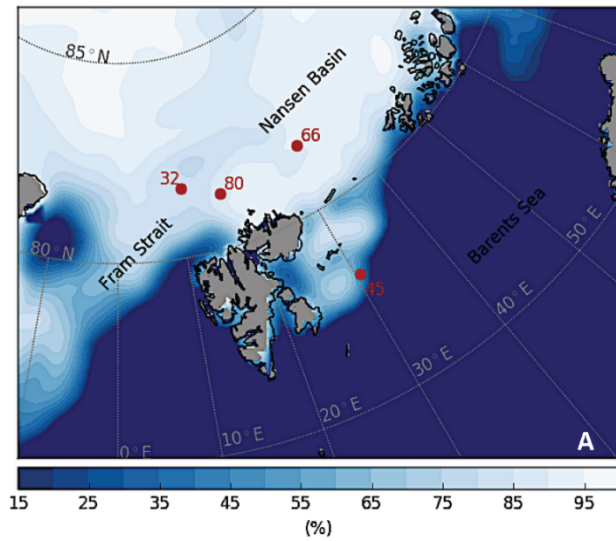
Fig. 1:
Study area with sample locations. A: Sea ice coverage at the station and time of sampling in %. B) Trajectories of the sea ice from which the cryogenic gypsum was released. Each trajectory starts where sea ice formed (black circles), and shows its drift until the time and place of sampling (white circles). The colour scale of the drift trajectories indicates the month in which the back-tracked sea ice was at any given position.

26

740
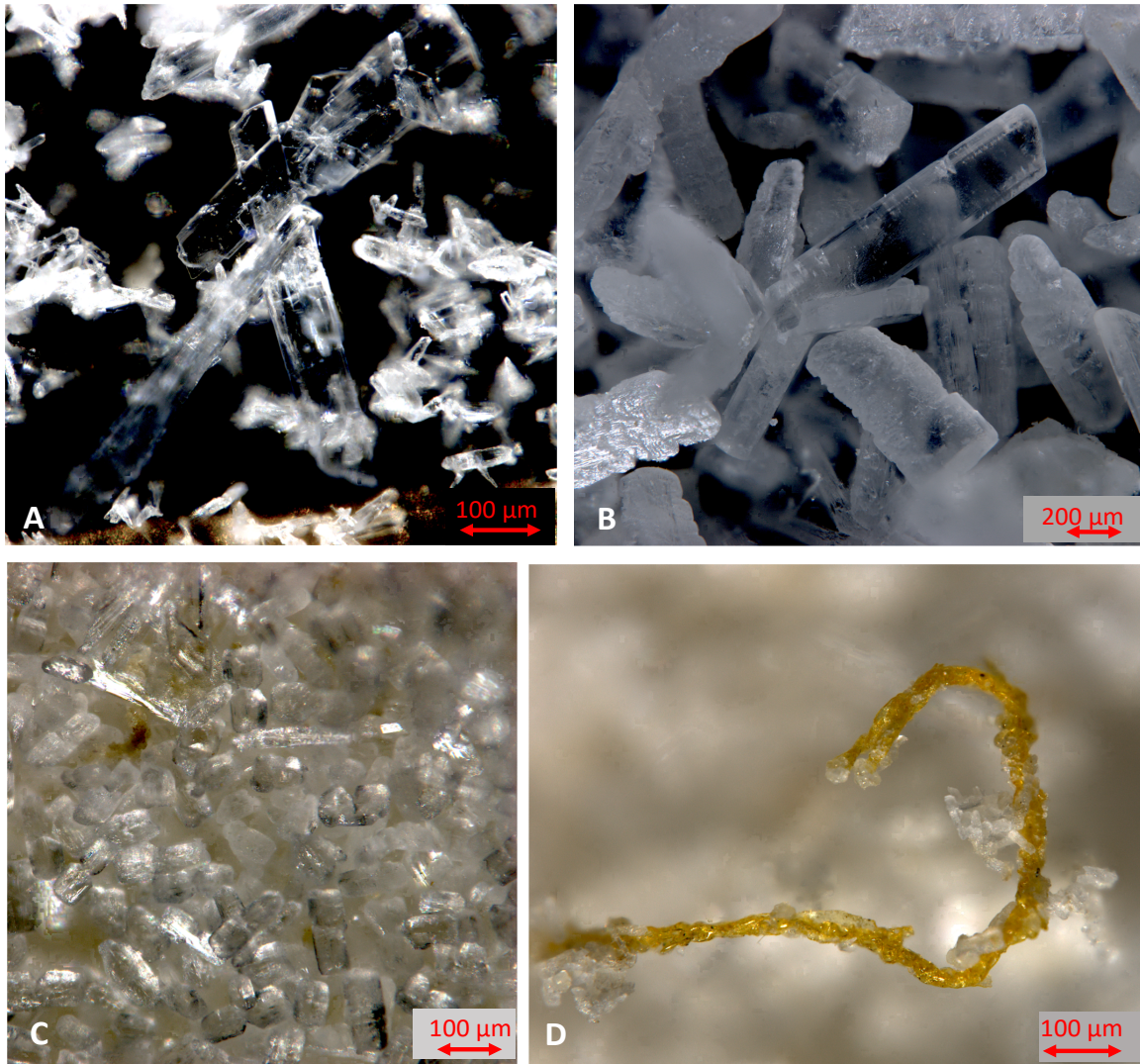
741   Fig. 2: Cryogenic gypsum crystals collected during Polarstern expedition PS106-1 from the

742   upper water column. A) Crystals collected from station 66 at 5 m water depth. B) Crystals

743   collected from station 66 at 0 m water depths. C) Crystals collected from station 45 at 10 m

744   water depth. D) Crystals collected from station 45 at 10 m water depths entangled in an algae

745   filament.

746

747

748
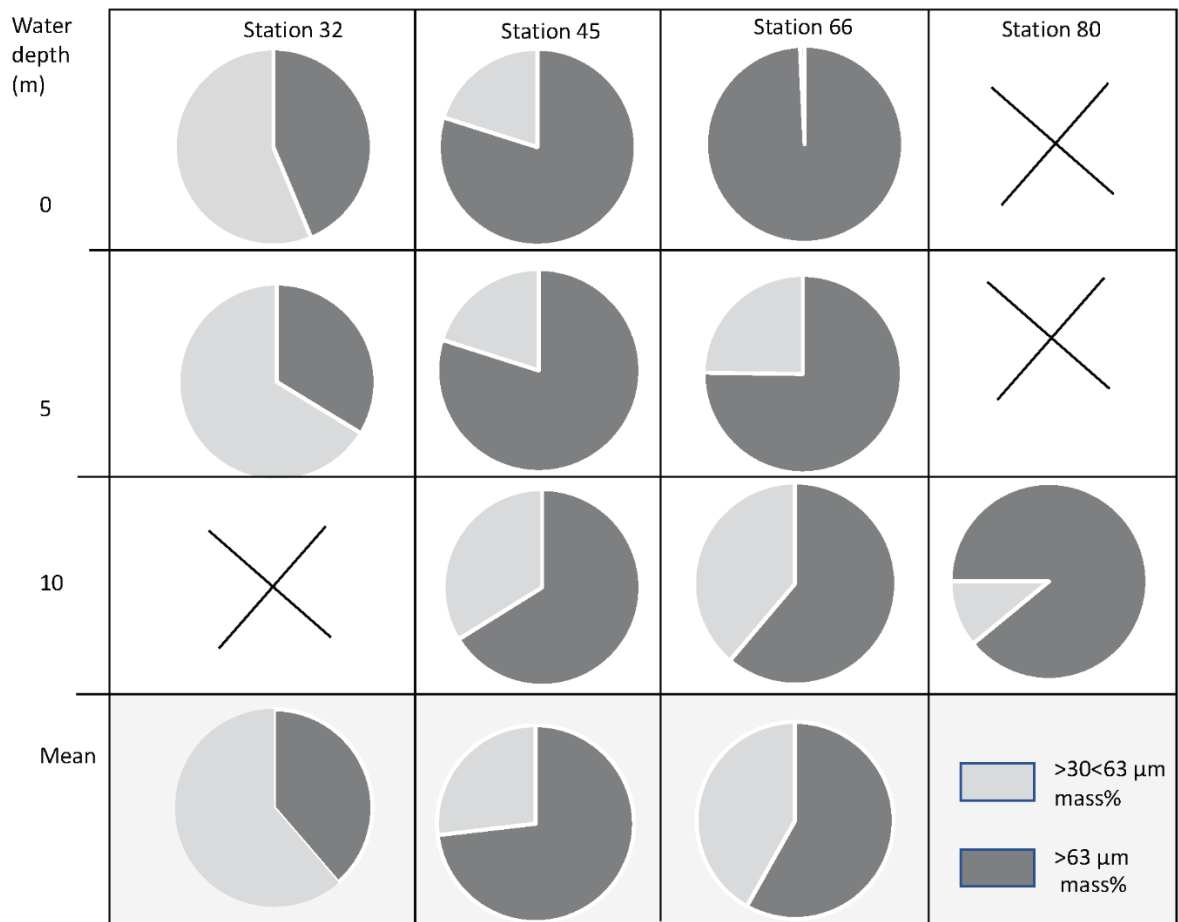
749

750   Fig. 3: Proportional mass (%) of cryogenic gypsum for the size fractions >30<63 μm and >63

751   μm for all ROV samples.

752
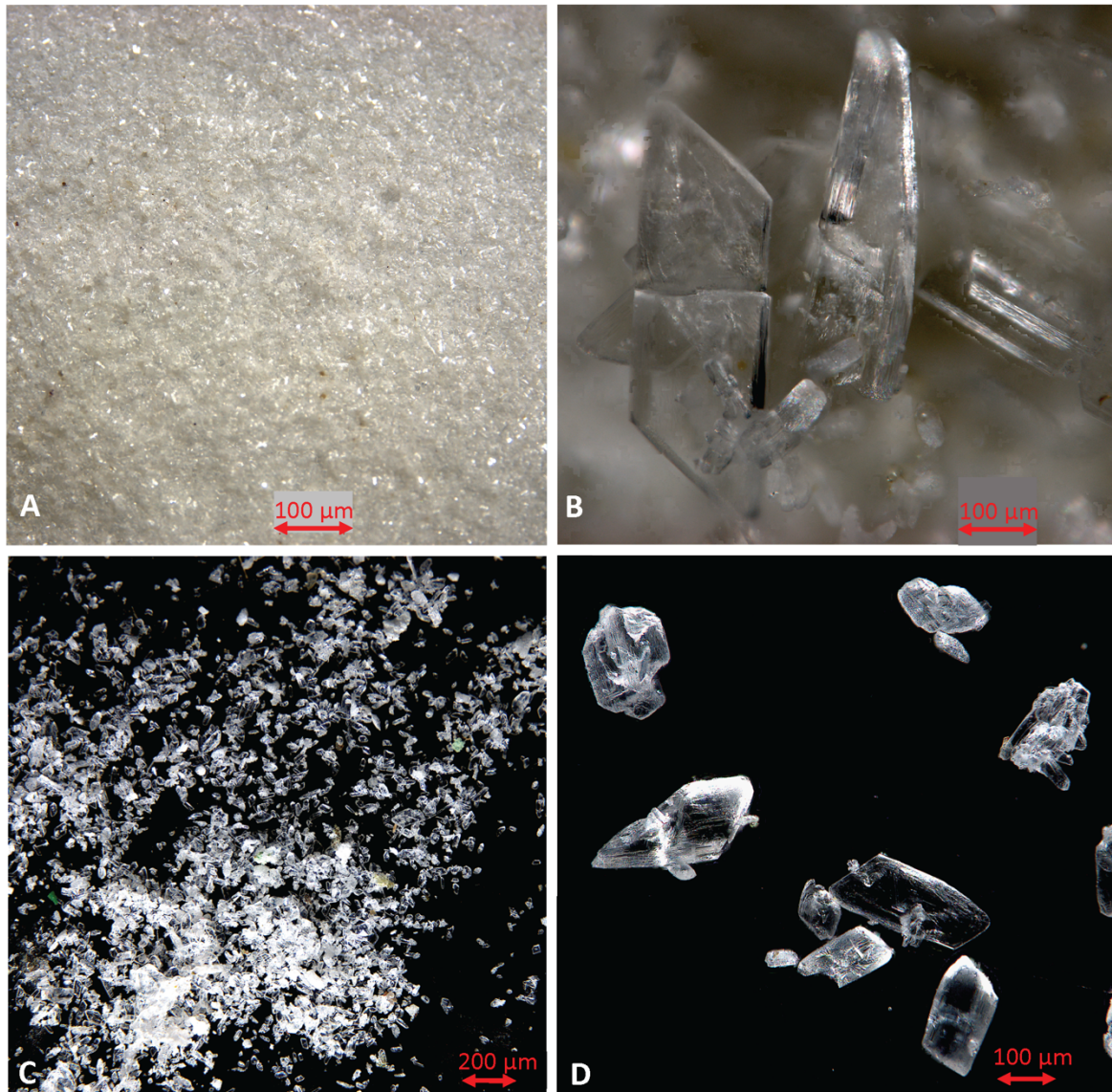
753
754 Fig. 4: Comparison of cryogenic gypsum crystals collected from the water column at station
755 PS45 (10 m water depth) (A-B) with crystals retrieved from an ice-core collected above the
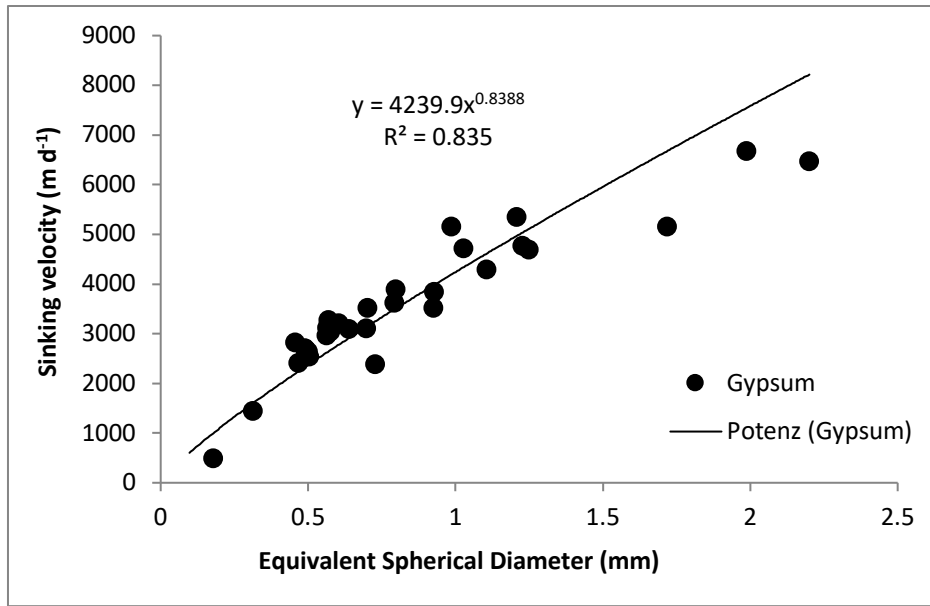756 ROVnet sampling area (C-D).
757
758
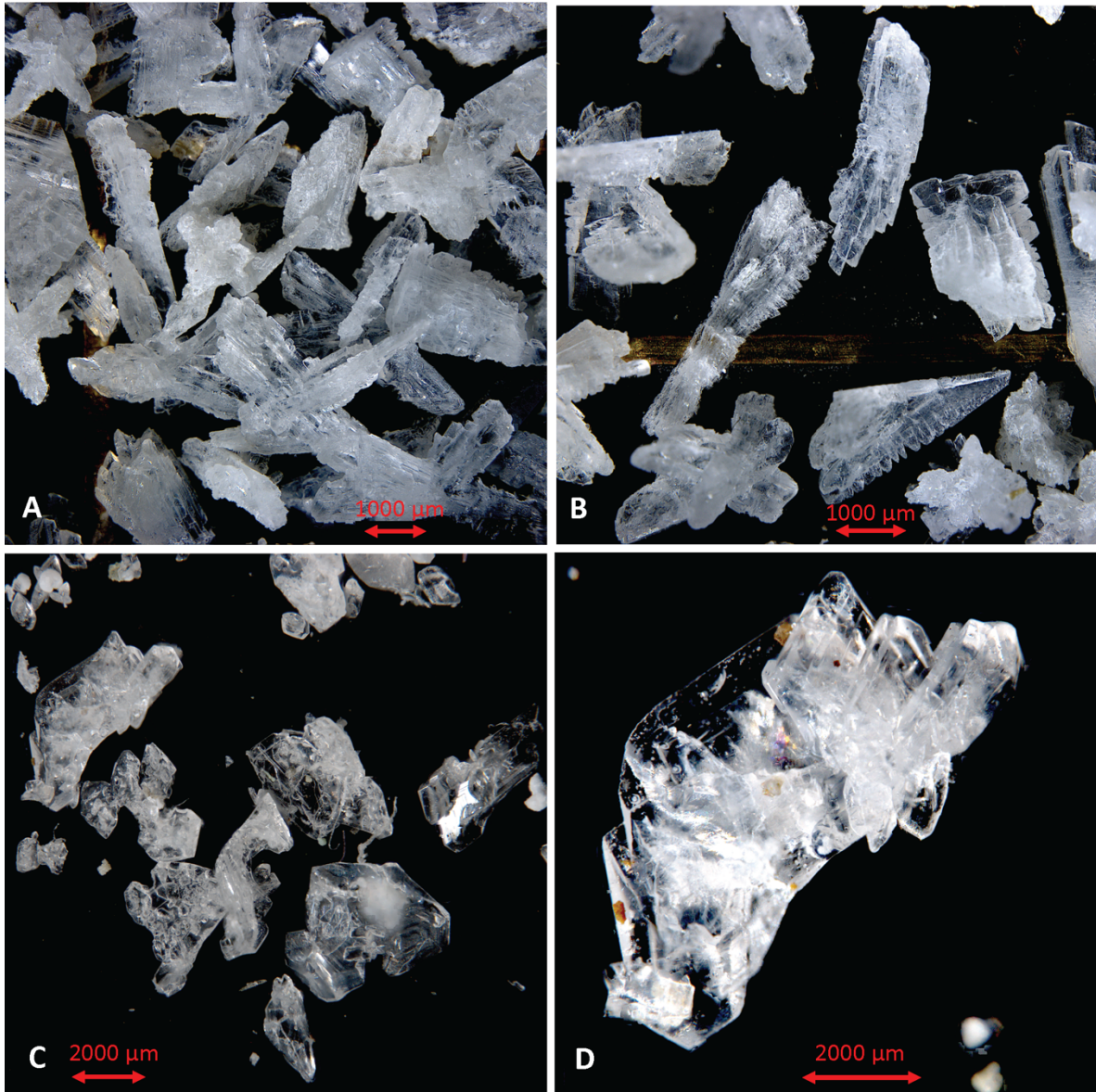
Fig. 5: Comparison of cryogenic gypsum crystals collected from the water column at station PS80-2 (10 m water depth) (A-B) with crystals retrieved from an ice-core collected above the ROVnet sampling area (C-D).
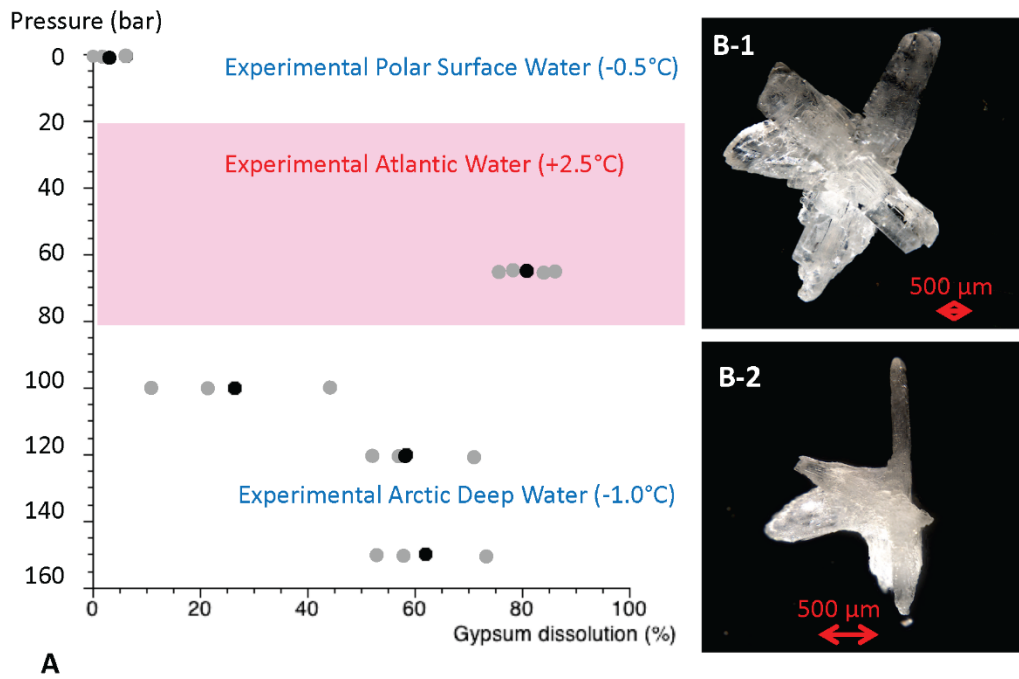
Figure 6: Results from cryogenic gypsum dissolution experiments. A) Graph showing the position of the simulated Arctic water masses in respect to pressure and temperature and how much gypsum (%) was dissolved on average over a 24-hours lasting exposure to such pressure and temperature conditions. Grey dots indicate the values from each aquarium, black dots the mean per experiment. B-1) Cryogenic gypsum crystal of the 120 bar-experiment before exposure. B-2) The same cryogenic gypsum crystal of the 120 bar-experiment after 24 hours.

The chart shows a scatter plot with the equation:

$$y = 4239.9x^{0.8388}$$
$$R^2 = 0.835$$

Y-axis: Sinking velocity (m d^{-1})

X-axis: Equivalent Spherical Diameter (mm)

Legend: ● Gypsum, — Potenz (Gypsum)

775

776 Fig. 7: Sinking velocity of cryogenic gypsum crystals plotted against equivalent spherical

777 diameter (ESD).

778
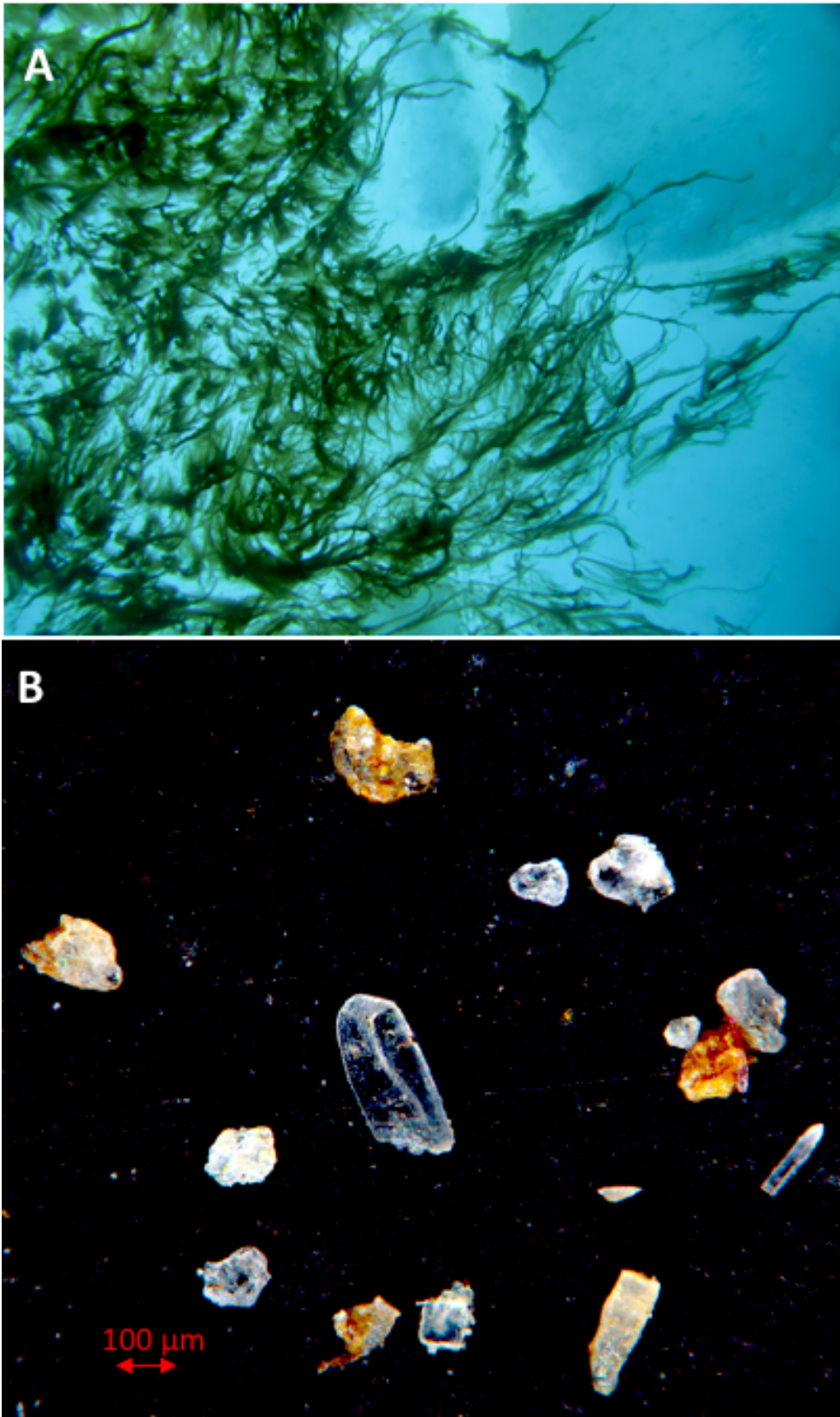
Fig. 8: Living *Melosira arctica* curtains hanging from ice flows during the PS106 expedition (photo taken by M. Nicolaus and C. Katlein). Cryogenic gypsum isolated from *Melosira arctica* (PS106-1, station 21(Peeken, 2018)).

784

Author Contributions:

J.W., H.F: and M.I. designed this study. J.W. lead the writing of this manuscript and
performed gypsum sample preparation and analysis. H.F., I.P., C.K., G.C., M.N. acquired
ROVnet and ice samples in the field. M.I. measured crystal settling velocities. T.K. performed
the backtracking analysis. All authors contributed to the writing and editing of the manuscript